Classification of Chaotic Squeak And Rattle Vibrations By CNN Using Recurrence Pattern

Jaehyeon Nam
Inha University Department of Mechanical Engineering
Jaeyoung Kang (kangj@inha.ac.kr)
Inha University Department of Mechanical Engineering https://orcid.org/0000-0003-1483-0278

Research Article

Keywords: Squeak, Rattle, Convolutional Neural Network, Lyapunov exponent, Chaos, Recurrence patterns

Posted Date: August 9th, 2021

DOI: https://doi.org/10.21203/rs.3.rs-629564/v1

Version of Record: A version of this preprint was published at Sensors on December 2nd, 2021. See the published version at https://doi.org/10.3390/s21238054.

Classification of chaotic squeak and rattle vibrations by CNN using recurrence pattern

Jaehyeon Nam[1]

Jaeyoung Kang[2,*]

jaehyeon@inha.edu

Corresponding author*: Jaeyoung Kang(kangj@inha.ac.kr)

Department of Mechanical Engineering, Inha University, 100 Inha-ro, Michuhol-gu, Incheon, Korea[1,2]

ABSTRACT: The chaotic squeak and rattle (S&R) vibrations in mechanical systems were classified by deep learning. The rattle, single-mode, and multi-mode squeak models were constructed to generate chaotic S&R signals. The repetition of nonlinear signals generated by them was visualized using an unthresholded recurrence plot and learned using a convolutional neural network (CNN). The results showed that even if the signal of the S&R model is chaos, it could be classified. The accuracy of the classification was verified by calculating the Lyapunov exponent of the vibration signal. The numerical experiment confirmed that the CNN classification using nonlinear vibration images as the proposed procedure has more than 90% accuracy. The chaotic status and each model can be classified into six classes.

keywords: Squeak; Rattle; Convolutional Neural Network; Lyapunov exponent; Chaos; Recurrence patterns

1. Introduction

Chaotic squeak and rattle (S&R) vibrations are a significant factor for evaluating the quality of automotive parts. Early S&R was detected with a find-and-fix approach by a subjective evaluation from engineers. Therefore, highly skilled experts are needed to detect S&R. In addition, the evaluation was made subjectively because of the differences in training and expertise and the use of different measurement tools. For this reason, an objective tool is needed for quantitative measurements. On the other hand, the S&R indices developed for such an evaluation must define the threshold value of the index, and the threshold value is based on a subjective evaluation [1-4]. In addition, S&R problems occurring in mechanical systems are challenging to analyze because they include extreme nonlinearities, such as impact and friction [5-9].

Squeak is a self-excited vibration caused by friction that frequently occurs in automobile brakes, artificial hip joints, and gear systems [8,10,11]. Many studies have examined the vibration instability caused by friction based on an analysis of brake squill noise. The method to solve these problems was studied mainly by analyzing the instability using vibration equations, including nonlinearity of friction and linear stability through the linearization of nonlinear terms. On the other hand, the

linearized approach can only be investigated near equilibrium. Kang [8] described complex models, such as instability caused by friction curves, modal coupling instability, gyroscopic, and friction damping occurring in automobile disc brake systems. They also analyzed the influence of squeal. Nam et al. [10] investigated the vibration instability in the lead screw system experimentally and analyzed the instability mechanism using the finite element method (FEM). Ouenzerfi et al. [11] examined the frictional instability occurring in an artificial hip joint and investigated the instability through a detailed FEM. In addition, the friction force is expressed as a function of the velocity in the dynamic instability of the friction-induced model. Higher-order nonlinear problems, such as chaos, were described because the model includes extreme nonlinearity in the creep section [12-16]. Kang [15] used a two-degree-of-freedom friction model to show the chaotic phenomenon is generated by self-excited vibrations and investigated the parameters that create chaos.

Rattle can cause chaos due to extreme discontinuity caused by the impact force, including vibrations due to the impact vibrations induced by the excitation. For this reason, the dynamics of impact motion have been studied extensively for a study of chaos. Serweta et al. [18, 19] examined the chaotic characteristics by calculating the Lyapunov exponent of an impact oscillator with symmetrical soft stops and rigid stop. Kang [20] analyzed the chaotic factors by calculating the Lyapunov exponent for the truncated number of modes of the impact beam under a distributed contact using the continuum beam model.

In addition to the theoretical approach, the analysis of such a nonlinear vibration signal has been performed using a visualization method and a quantified index. A general signal analysis method takes an FFT in the time series and analyzes the dynamic characteristics in the frequency domain. Furthermore, dynamical characteristics were examined through the trajectory of the attractor in the phase space. As many studies on signal analysis have been carried out, signal visualization methods, such as Gauss wavelets [21, 22] and a recurrence plot (RP), have been developed. Marwan et al. [23] introduced various RP methods to visualize the dynamic characteristics in a complex system. RP is a power tool that visualizes and analyzes the recurrence characteristics of dynamic systems. In addition, recurrence can be visualized efficiently and developed formally using a matrix. The reciprocal of the longest diagonal of an RP is proportional to the largest Lyapunov exponent. This shows that RP can express both the recurrence and chaos characteristics well. An RP is represented on the reconstructed phase space that is determined using the time delay method [24-27]. Recurrence quantification analysis (RQA) can quantify the repetition characteristics through indices expressed as found in the recurrence rate (RR), the determinism (DET), and the average diagonal line length based on the RP. RQA is a good technique for quantifying recurrence properties, but the results are presented only in indices [23]. In addition, higher-order spectrum analysis (HOSA) and clustering techniques are used to analyze various methods, including high-dimensional nonlinearity [28].

Dynamics problems involving extreme nonlinearities, such as S&R, can be accompanied by chaos. The most accurate way to determine chaos is the Lyapunov exponent. Wolf et al. described a method called the spectrum of the largest Lyapunov exponent. A calculation algorithm was also developed [17], and chaos could be determined by parameter analysis. On the other hand, this algorithm cannot be applied in nonlinear dynamical systems, including discontinuities, and can only be used in smooth dynamical systems. In contrast, Muller's algorithm can be applied to a non-smooth dynamical system

through an indicator function and transition condition [16]. Determining the chaos through the Lyapunov exponents is advantageous if the governing equation for the system is known or the available observations are very long [29].

Recently, with the rapid development of artificial intelligence, many algorithms using machine learning have been developed. In particular, for image classification, numerous CNN models based on a convolutional neural network (CNN) have been established, and ResNet, which was released in 2015, transcends human cognitive ability [30]. Hsueh et al. [31] showed that the fault signal of a motor through the experiment could be classified in binary by a CNN. Nam et al. [32] reported that, even if the vibration signal includes discontinuous nonlinearities, such as impact, the chaotic signal can be classified by a CNN using the image visualized with an unthresholded RP. On the other hand, it only performed a dichotomous classification for chaos and non-chaos. Therefore, the binary classification study was extended to perform a multi-class classification of chaotic S&R vibration signals.

This study examined whether the rattle and squeak signals can be classified through a CNN, even if they are chaotic, by applying a signal visualization technique. Because CNN is an image-based classification technique, an RP-based dataset was constructed to express the repetition of a dynamic system quantitatively. A single-mode squeak, multi-mode squeak, and rattle model were built. A methodology that classifies six classes for the chaotic S&R model with high accuracy through a CNN is proposed.

2. Methods

In this study, a theoretical model of S&R vibration, a representative nonlinear vibration that can occur in a mechanical system, is used. Figure 1 presents the rattle model considering the mass, linear spring, nonlinear elastic contact, and damping. k is a linear spring coefficient. This system is excited with amplitude f_0 and excitation frequency ω_{ex}. As shown in Figure 1 (a), the distance from the impact surface at the static equilibrium position of the system is L. In addition, the nonlinear elastic model of the impact force was defined as Hertz's contact model [18, 19]. The coordinate x^r describes the vibration motion of the Rattle model at the static equilibrium position. Figure 1 (b) shows the impact force of Hertz's contact model for a relative displacement. All systems consider a mass m attached to a spring with a stiffness coefficient k and coefficient of viscous damping c.

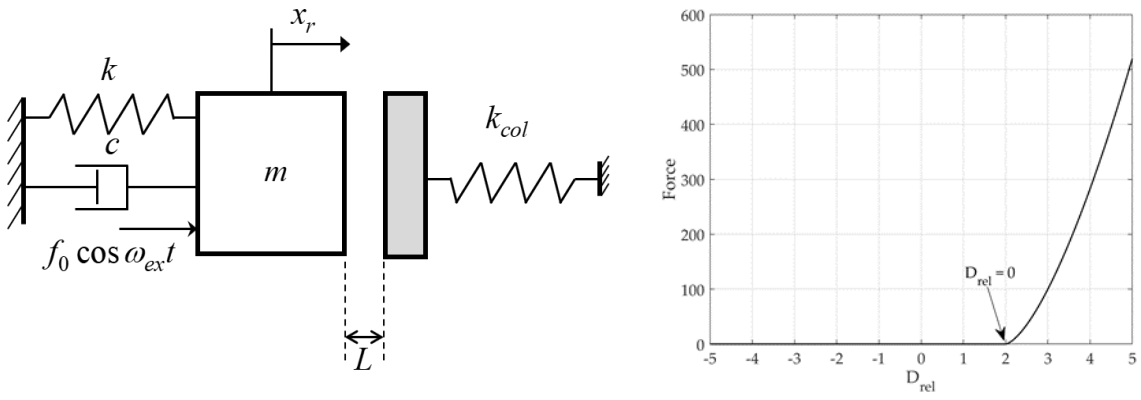

Figure1: Rattle model (a) 1-D model (b) impact force

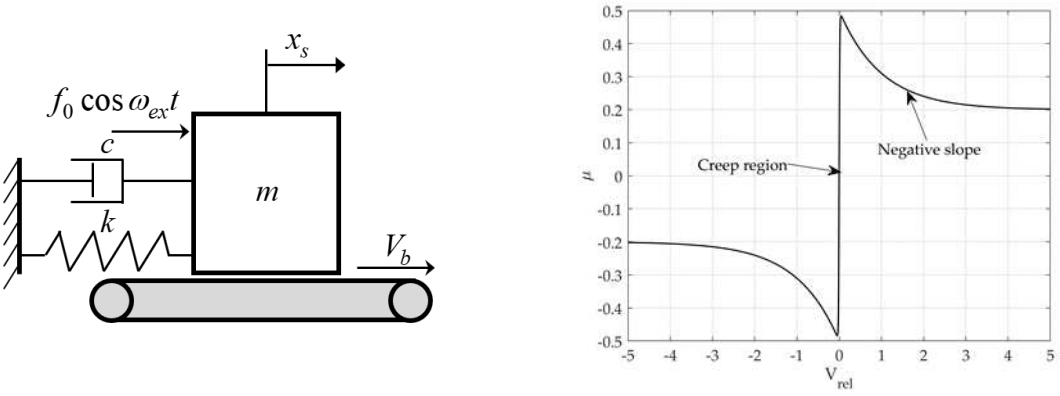

106
107 Figure2: Single-mode squeak model (a) 1-D model (b) friction-velocity curve

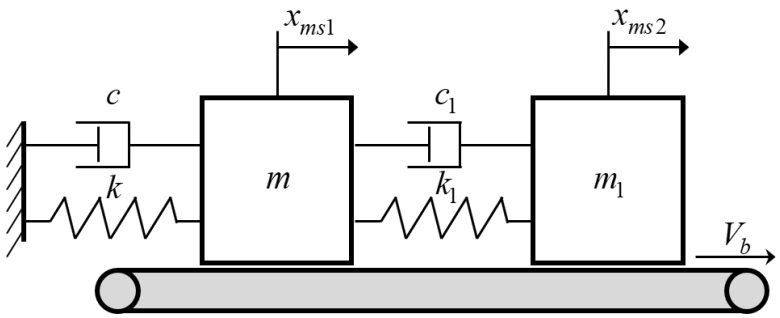

108

109 Figure3: Multi-mode squeak model

110 The single-mode squeak model is excited with the same amplitude f_0 and excitation frequency
111 ω_{ex} as the rattle model shown in Figure 2 (a). On the contact surface, a frictional force is generated by
112 the normal force and the relative velocity. The friction force includes the creep region and negative
113 slope for the sliding speed from Coulomb's law of friction, as shown in Figure 2(b). The multi-mode
114 squeak model has an added mass m_1, spring stiffness k_1 , and coefficient of viscous damping c_1,
115 and the frictional force generated by each mass is the same as that of the single-mode squeak model,
116 as shown in Figure 3.

117 For the rattle model shown in Figure 1 (a)

118 $$m\ddot{x}_r + c\dot{x}_r + kx_r = f_0 \cos \omega_{ex} t + F_c \tag{1}$$

119 where the contact model is the impact force by Hertz's nonlinear elastic model as follows:

120 $$\begin{aligned} F_c &= 0 && \text{if } x_r < L \\ F_c &= k_c (x_r - L)^{3/2} && \text{if } x_r \geq L \end{aligned} \tag{2}$$

121 Using the dimensionless time $\tau = t\sqrt{k/m}$ and the coordinate transformation $x_r(t) = X_r(\tau)$, the
122 dimensionless equation of motion can be written as

$$X_r'' + \beta X_r' + X_r = f_0 \cos\eta\tau + F_c \frac{1}{k} \tag{3}$$

where prime is differentiation for $\tau(\geq 0)$ and the dimensionless parameter is defined as $\Omega = \sqrt{k/m}$, $\eta = \omega_{ex}/\Omega$, $f_0 = F_0/k$, $\beta = \sqrt{c^2/mk}$, and $u = X_r/f_0$. Therefore, the dimensionless equation of motion for the rattle model can be written as

$$u'' + \beta u' + u = \cos\eta\tau + Hf_c \tag{4}$$

and the dimensionless form of the impact force is rewritten as follows:

$$\begin{aligned} f_c &= 0 && \text{if } u < r \\ f_c &= k_c(u-r)^{3/2} && \text{if } u \geq r \end{aligned} \tag{5}$$

Equation of motion for the rattle model is expressed in vector form as follows:

$$\mathbf{u} = \begin{bmatrix} u & u' \end{bmatrix}^{\mathbf{T}} \tag{6}$$

$$\mathbf{u}' = \mathbf{f}_r(\mathbf{u}),\ \mathbf{u}(0) = \mathbf{u}_0 \tag{7}$$

$$\mathbf{f}(\mathbf{u}) = \begin{bmatrix} u_2 \\ -\beta u_2 - u_1 + \cos(u_3) + Hf_c \\ \eta \end{bmatrix} \tag{8}$$

where H is the Heaviside function and $\mathbf{u}_0$ is the initial condition of the rattle model.

Equation (7) is a dynamic system with discontinuities involving the discontinuous impact effects in the rattle model. Therefore, it can be rewritten as follows from Muller's method that includes the instantaneous discontinuity of impact. Here $\tau = \tau_i$ is a discontinuous moment. Let $\mathbf{z}$ be a state variable $\mathbf{u}$ of the rattle model.

$$\tau_{i-1} < \tau < \tau_i:\ \mathbf{z}' = \mathbf{f}_i(\mathbf{z}),\ \mathbf{z}(\tau_{i-1}) = \mathbf{z}(\tau_{i-1}^+) \tag{9}$$

$$\tau = \tau_i:\ \mathbf{0} = \mathbf{h}(\mathbf{z}(\tau_i^-)) \tag{10}$$

$$\mathbf{z}(\tau_i^+) = \mathbf{g}(\mathbf{z}(\tau_i^-)) \tag{11}$$

$$\tau_i < \tau < \tau_{i+1}:\ \mathbf{z}' = \mathbf{f}_{i+1}(\mathbf{z}),\ \mathbf{z}(\tau_i) = \mathbf{z}(\tau_i^+) \tag{12}$$

The perturbed trajectory is given by

$$\tilde{\mathbf{z}}(\tau) = \mathbf{z}(\tau) + \delta\mathbf{z}(\tau) \tag{13}$$

$$\tilde{\tau}_i = \tau_i + \delta\tau_i \tag{14}$$

and the perturbed trajectory satisfies the following equation:

$$\tilde{\tau}_{i-1} < \tau < \tilde{\tau}_i : \ \tilde{\mathbf{z}}' = \mathbf{f}_i(\tilde{\mathbf{z}}), \ \ \tilde{\mathbf{z}}(\tilde{\tau}_{i-1}) = \tilde{\mathbf{z}}(\tilde{\tau}_{i-1}^{+}) \tag{15}$$

$$\tau = \tilde{\tau}_i : \ \mathbf{0} = \mathbf{h}(\tilde{\mathbf{z}}(\tilde{\tau}_i^{-})) \tag{16}$$

$$\tilde{\mathbf{z}}(\tilde{\tau}_i^{+}) = \mathbf{g}(\tilde{\mathbf{z}}(\tilde{\tau}_i^{-})) \tag{17}$$

$$\tilde{\tau}_i < \tau < \tilde{\tau}_{i+1} : \ \tilde{\mathbf{z}}' = \mathbf{f}_{i+1}(\tilde{\mathbf{z}}), \ \ \tilde{\mathbf{z}}(\tilde{\tau}_i) = \tilde{\mathbf{z}}(\tilde{\tau}_i^{+}) \tag{18}$$

where each interval of discontinuities is smooth. $\mathbf{h}(\mathbf{z})$ and $\mathbf{g}(\mathbf{z})$ are the indicator function, and the transition condition, respectively. The plus and minus signs denote the right- and left-sided limits, and

$$\delta\tau_i = \tilde{\tau}_i - \tau_i = -\frac{D\mathbf{h}(\mathbf{z}_i^{-})\delta\mathbf{z}_i^{-}}{D\mathbf{h}(\mathbf{z}_i^{-})\mathbf{f}_i(\mathbf{z}_i^{-})} \tag{19}$$

$$\delta\mathbf{z}_i^{+} = D\mathbf{g}(\mathbf{z}_i^{-})\delta\mathbf{z}_i^{-} + [D\mathbf{g}(\mathbf{z}_i^{-})\mathbf{f}_i(\mathbf{z}_i^{-}) - \mathbf{f}_{i+1}(\mathbf{z}_i^{+})]\delta\tau_i \tag{20}$$

in which

$$D\mathbf{h}(\mathbf{z}_i^{-}) = \left.\frac{\partial \mathbf{h}(\mathbf{z})}{\partial \mathbf{z}}\right|_{\mathbf{z}=\mathbf{z}_i^{-}}, \ \ D\mathbf{g}(\mathbf{z}_i^{-}) = \left.\frac{\partial \mathbf{g}(\mathbf{z})}{\partial \mathbf{z}}\right|_{\mathbf{z}=\mathbf{z}_i^{-}} \tag{21}$$

are the Jacobian matrix of indicator function and transition condition at point $\mathbf{z}_i^{-}$, respectively, where $\mathbf{z}_i^{-} = \mathbf{z}(\tau_i^{-})$ and $\mathbf{z}_i^{+} = \mathbf{z}(\tau_i^{+})$. For an impact oscillator with Hertz's model of contact, the Jacobian matrix of the transition condition and indicator function becomes the following matrix [18]:

$$D\mathbf{h}(\mathbf{z}_i^{-}) = \begin{bmatrix} 1 & 0 & 0 \end{bmatrix}^{\mathbf{T}}, \ \ D\mathbf{g}(\mathbf{z}_i^{-}) = \mathbf{I} \tag{22}$$

Therefore, the deviated trajectory can be written as

$$\delta\mathbf{z}' = \left.\frac{\partial \mathbf{f}}{\partial \mathbf{z}}\right|_{\mathbf{z}=z_i} \cdot \delta\mathbf{z} + O_{(2)}, \ \ \delta\mathbf{z}(\tau_0) = \delta\mathbf{z}_0 \tag{23}$$

By letting $\delta\mathbf{z} = \left[\mathbf{\Phi}_\tau(\mathbf{z}_0)\right]\delta\mathbf{z}_0$ substitute into the perturbation equation (23), $\delta\mathbf{z}_i^{+}$ at the discontinuous region is estimated using Equation (20). The variation equation is also calculated at the same time as

$$\left[\mathbf{\Phi}'_\tau(\mathbf{z}_0)\right] = [D_z\mathbf{f}][\mathbf{\Phi}_\tau(\mathbf{z}_0)], \ \ [\mathbf{\Phi}_{\tau_0}(\mathbf{z}_0)] = [\mathbf{I}] \tag{24}$$

where $[D_z\mathbf{f}]$, $[\mathbf{I}]$, and $\left[\mathbf{\Phi}_\tau(\mathbf{z}_0)\right]$ denote the Jacobian matrix, identity matrix, and solution of the variational equation, respectively.

For the single-mode squeak model shown in figure 2 (a)

$$m\ddot{x}_s + c\dot{x}_s + kx_s = f_0 \cos\omega_{ex} t + F_\mu^{x_s} \tag{25}$$

where $F_\mu^{x_s}$ is the friction force. The friction force of the single-mode squeak model is expressed as α, and h are the control parameters that determine the negative slope. μ_s and μ_k are the static and dynamic friction coefficients, respectively.

$$F_\mu^{x_s} = \tanh(\alpha(V_b - \dot{x}_s))\left\{\mu_k + (\mu_s - \mu_k)\exp\left(-h\left|V_b - \dot{x}_s\right|\right)\right\} N \tag{26}$$

Using the dimensionless time $\tau = t\sqrt{k/m}$ and the coordinate transformation $x_s(t) = X_s(\tau)$, the dimensionless equation of motion can be written as

$$X_s'' + \beta X_s' + X_s = f_0 \cos\eta\tau + \frac{1}{k} F_\mu^{x_s} \tag{27}$$

where prime is the differentiation for $\tau(\geq 0)$, and the dimensionless parameters were defined as $\Omega = \sqrt{k/m}$, $\eta = \omega_{ex}/\Omega$, $f_0 = F_0/k$, $\beta = \sqrt{c^2/mk}$, and $u = X_r/f_0$. Therefore, the dimensionless friction force of the single-mode squeak model can be expressed as

$$f_\mu^v = \tanh\left(\alpha\left(V_b - v'\right)\right)\left\{\mu_k + (\mu_s - \mu_k)\exp\left(-h\left|V_b - v'\right|\right)\right\} n_0 \tag{28}$$

where $\alpha\Omega f_0 \to \alpha$, $V_b/\Omega f_0 \to V_b$, $h\Omega f_0 \to h$, and $N/kf_0 = n_0$ are dimensionless parameters. Therefore, the dimensionless equation of motion for the single-mode squeak model can be written as

$$v'' + \beta v' + v = \cos\eta\tau + f_\mu^v \tag{29}$$

The equation of motion for the single-mode squeak model is expressed in vector form:

$$\mathbf{v} = \begin{bmatrix} v & v' \end{bmatrix}^{\mathbf{T}} \tag{30}$$

$$\mathbf{v}' = \mathbf{f}_s(\mathbf{v}),\ \mathbf{v}(0) = \mathbf{v}_0 \tag{31}$$

$$\mathbf{f}_s(\mathbf{v}) = \begin{bmatrix} v_2 \\ -\beta v_2 - v_1 + \cos(v_3) + f_\mu^v \\ \eta \end{bmatrix} \tag{32}$$

where $\mathbf{v}_0$ is the initial condition of the single-mode squeak model.

For the multi-mode squeak model shown in figure 3,

$$\begin{aligned} m\ddot{x}_{ms1} + (c + c_1)\dot{x}_{ms1} - c_1\dot{x}_{ms2} + (k + k_1)x_{ms1} - k_1 x_{ms2} &= F_\mu^{x_{ms1}} \\ m_1\ddot{x}_{ms2} - c_1\dot{x}_{ms1} + c_1\dot{x}_{ms2} - k_1 x_{ms1} + k_1 x_{ms2} &= F_\mu^{x_{ms2}} \end{aligned} \tag{33}$$

where F_μ^{ms1} and F_μ^{ms2} are the friction forces acting on each mass. The friction force of the multi-mode squeak model is expressed as

$$F_{\mu}^{x_{ms1}} = \tanh(\alpha(V_b - \dot{x}_{ms1}))\left\{\mu_k + (\mu_s - \mu_k)\exp\left(-h\left|V_b - \dot{x}_{ms1}\right|\right)\right\} N \tag{34}$$

$$F_{\mu}^{ms2} = \tanh(\alpha(V_b - \dot{x}_{ms2}))\left\{\mu_k + (\mu_s - \mu_k)\exp\left(-h\left|V_b - \dot{x}_{ms2}\right|\right)\right\} N \tag{35}$$

Using the dimensionless time $\tau = t\sqrt{k/m}$ and the coordinate transformation $x_{ms1}(t) = X_{ms1}(\tau)$ and $x_{ms2}(t) = X_{ms2}(\tau)$, the dimensionless equation of motion can be expressed as

$$\begin{aligned} &X_{ms1}^{''} + (\beta + \beta_1) X_{ms1}^{'} - \beta_1 X_{ms2}^{'} + (1+\gamma) X_{ms1} - \gamma X_{ms2} = \frac{1}{k} F_{\mu}^{x_{ms1}} \\ &X_{ms2}^{''} - \sigma\beta_1 X_{ms1}^{'} + \sigma\beta_1 X_{ms2}^{'} - \sigma\gamma X_{ms1} + \sigma\gamma X_{ms2} = \sigma\frac{1}{k} F_{\mu}^{x_{ms2}} \end{aligned} \tag{36}$$

where prime is the differentiation with respect to $\tau(\geq 0)$, and the dimensionless parameter was defined as $\Omega = \sqrt{k/m}$, $\eta = \omega_{ex}/\Omega$, $f_0 = F_0/k$, $\beta = \sqrt{c^2/mk}$, $\beta_1 = \sqrt{c_1^2/mk}$, $\gamma = k_1/k$, $\sigma = m/m_1$, $w = X_{ms1}/f_0$, and $s = X_{ms2}/f_0$. Therefore, the dimensionless friction force of the multi-mode squeak model can be rewritten as

$$f_{\mu}^{w} = \tanh\left(\alpha\left(V_b - w^{'}\right)\right)\left\{\mu_k + (\mu_s - \mu_k)\exp\left(-h\left|V_b - w^{'}\right|\right)\right\} n_0 \tag{37}$$

$$f_{\mu}^{s} = \tanh\left(\alpha\left(V_b - s^{'}\right)\right)\left\{\mu_k + (\mu_s - \mu_k)\exp\left(-h\left|V_b - s^{'}\right|\right)\right\} n_0 \tag{38}$$

where $\alpha\Omega f_0 \to \alpha$, $V_b/\Omega f_0 \to V_b$, $h\Omega f_0 \to h$ and $N/kf_0 = n_0$ are dimensionless parameters. Therefore, the dimensionless equation of motion for the simple model can be expressed as

$$\begin{aligned} &w'' + (\beta + \beta_1) w' - \beta_1 s' + (1+\gamma) w - \gamma s = f_{\mu}^{w} \\ &s'' - \sigma\beta_1 w' + \sigma\beta_1 s' - \sigma\gamma w + \sigma\gamma s = f_{\mu}^{s} \end{aligned} \tag{39}$$

The equation of motion for the multi-mode squeak model is expressed in vector form as follows:

$$\mathbf{w} = \begin{bmatrix} w & w' & s & s' \end{bmatrix}^{\mathbf{T}} \tag{40}$$

$$\mathbf{w}' = \mathbf{f}_{ms}(\mathbf{w}),\ \mathbf{w}(0) = \mathbf{w}_0 \tag{41}$$

$$\mathbf{f}_{ms}(\mathbf{w}) = \begin{bmatrix} w_2 \\ -(\beta+\beta_1)w_2 + \beta_1 s_2 - (1+\gamma)w_1 + \gamma s_1 + f_{\mu}^{w} \\ s_2 \\ \sigma\left(\beta_1 w_2 - \beta_1 s_2 + \gamma w_1 - \gamma s_1 + f_{\mu}^{s}\right) \end{bmatrix} \tag{42}$$

where $\mathbf{w}_0$ is the initial condition of the multi-mode squeak model.

Because the squeak models are a dynamic system without discontinuities, Equations (9) – (22) are unnecessary. Therefore, the Lyapunov exponent of the squeak model can be obtained directly from

the eigenvalue of the variation equation (24).

The Lyapunov exponents can be defined as

$$\lambda_i = \lim_{\tau\to\infty} \frac{1}{\tau} \ln\left|m_i(\tau)\right| \tag{43}$$

where $m_i(t)$ are the eigenvalues of Equation (24). On the other hand, the definition cannot be used directly in the numerical calculation. If there is a considerable time, the variation equations tend to be the ill-condition [18]. Therefore, the spectrum of the Lyapunov exponent for the linearized equation was estimated using Wolf's algorithm via the QR-factorization orthonormalization [33].

As mentioned earlier, in this study, an image of a dynamic signal was constructed based on the RP that visualized the dynamic characteristics most effectively. The corresponding RP is based on the following recurrence matrix as follows:

$$\mathbf{RP}_{i,j} = H\left(\varepsilon - \left\|\mathbf{z}_i - \mathbf{z}_j\right\|\right), \quad i, j = 1,...,N \tag{44}$$

where $\mathbf{RP}_{i,j}$ is called the RP or threshold RP. $\|\cdot\|$ is an L-2 norm; N is the measured points, and $\{\mathbf{z}_i\}_{i=1}^{N}$ is trajectories of a system in its phase space. ε is the threshold. The threshold is a critical parameter that can be obtained differently depending on the system, but it was quantified probabilistically ($\varepsilon > 5\sigma$) by Thiel et al. [34]. Therefore, an unthresholded RP without the influence of the threshold can be expressed as

$$\mathbf{RP}_{i,j}^{un} = \left\|\mathbf{z}_i - \mathbf{z}_j\right\|, \quad i, j = 1,...,N \tag{45}$$

Here the element of phase space indicates the possible state of the system for the time-evolution law. In such a case, the phase space needs to be reconstructed. The method for reconstruction is generally conducted using the time delay method. Thus, the reconstructed state variable can be expressed as

$$\mathbf{z}_i \to \hat{\mathbf{z}}_i = \sum_{j=1}^{m} q_{i+(j-1)\nu}\mathbf{e}_j \tag{46}$$

where $q_i = q(i\Delta\tau)$, $\Delta\tau$, m, ν, and $\mathbf{e}_j$ are the discrete-time series, sampling rate, embedding dimension, time delay, and unit vectors, respectively. The reconstruction does not change the dynamic properties, and the reconstructed phase space can be expressed through an appropriately selected embedding dimension and time delay. In general, the time delay can be selected appropriately using the Mutual information method.

During time-delay reconstruction, all self-crossing trajectories in the dimension DA of the attractor can disappear when the embedding dimension D>2DA is set. On the other hand, it is imperative to determine the minimum embedding dimension to minimize the Lyapunov exponents and computational calculations from a physical perspective. From Equation (45), in dimension d, $\mathbf{z}_r$ is the r^{th} nearest neighbor of $\mathbf{z}$, and the square of the Euclidean distance between the two vectors is

$$R_d^2(i,r) = \sum_{e=0}^{\nu-1} \left[q_{(i+e\nu)} - q_{r,(i+e\nu)} \right]^2 \tag{47}$$

Here, as the time delay embedding extends from dimension d to dimension $d+1$, the Euclidean distance between the r[th] neighbors for dimension $d+1$ can be written as follows:

$$R_{d+1}^2(i,r) = R_d^2(i,r) + \left[q_{(i+e\nu)} - q_{r,(i+e\nu)} \right]^2 \tag{48}$$

where the error for the minimum embedding dimension can be determined from the rate of change of the Euclidean distance.

$$\sqrt{\frac{R_{d+1}^2(i,r) - R_d^2(i,r)}{R_{d+1}^2(i,r)}} > R_{tol} \tag{49}$$

where R_{tol} is the threshold. Kennel et al. [25] reported that false neighbors could be identified clearly in $R_{tol} \geq 10$. Another condition for determining false neighbors defined based on the actual value of $R_d(i) \equiv R_d(i, r=1)$ is similar to the standard variation R_A of the attractor using finite data of the noisy signal. Thus, the Euclidean distance for the dimension $d+1$ becomes $R_{d+1}(i) \approx 2R_A$, and the second criterion for determining false neighbors can be written as

$$\frac{R_{d+1}(i)}{R_A} > A_{tol} \tag{50}$$

Therefore, the minimum embedding dimension can be obtained by discriminating as false neighbors under the conditions in Equations (49) and (50).

Furthermore, the classified features were visualized through Class Activation Mapping (CAM) [35]. The procedure for CAM is as follows:

$$F^k = \sum_{x,y} f_k(x,y) \tag{51}$$

where $f_k(x,y)$ represents the activation of the k th unit of the last convolutional layer at the spatial location (x,y). Therefore, the value obtained by Global Average Pooling (GAP) on the k[th] unit becomes F^k. Accordingly, the input softmax for c classes is as follows:

$$S_c = \sum_k w_k^c \sum_{x,y} f_k(x,y) = \sum_k \sum_{x,y} w_k^c f_k(x,y) \tag{52}$$

where w_k^c is the weight corresponding to class c for k units, the learned weight represents an optimized model for class c. The output probability of softmax for class c is as follows:

$$P_c = \frac{e^{S_c}}{\sum_c e^{S_c}} \tag{53}$$

Therefore, CAM for the class c is defined, and the elements on each space are given as follows:

$$M_c(x, y) = \sum_k w_k^c f_k(x, y) \tag{54}$$

Finally, the features of the learning result using CNN can be visualized as a heat map using Equation (53).

3. Results

For preliminary analysis, the Rossler model, a representative chaotic system, was used [36]. The Rossler model has already been studied extensively. It is a simple chaotic vibration system because it can produce a section that always vibrates in response to a parameter change. c is selected as the control parameter. The other parameters are $a = 0.2$ and $b = 0.2$, and the initial condition is $\mathbf{q}(0) = \begin{bmatrix} 1 & 1 & 1 \end{bmatrix}^{\mathbf{T}}$.

$$\dot{\mathbf{s}} = \mathbf{f}(\dot{\mathbf{s}}) = \begin{bmatrix} -s_2 - s_3 \\ s_1 + a s_2 \\ b + s_3(s_1 - c) \end{bmatrix} \tag{55}$$

Figure 4 presents the signal s_1 for the control parameters of the Rossler model. Figure 4 (a) is a time series analysis for $c = 3.5$ (dash line) and $c = 10$ (solid line). Figure 4 (b) shows the corresponding phase space. $c = 3.5$ shows a clear period-2 in phase space; $c = 10$ shows the trajectory in the phase space and the aperiodic infinite trajectory in a finite boundary. On the other hand, the chaos cannot be identified clearly as a phase plot. To determine chaos, the Lyapunov exponents need to be calculated. Figure 5 presents the flow chart of the proposed methodology for applying signal classification using deep learning.

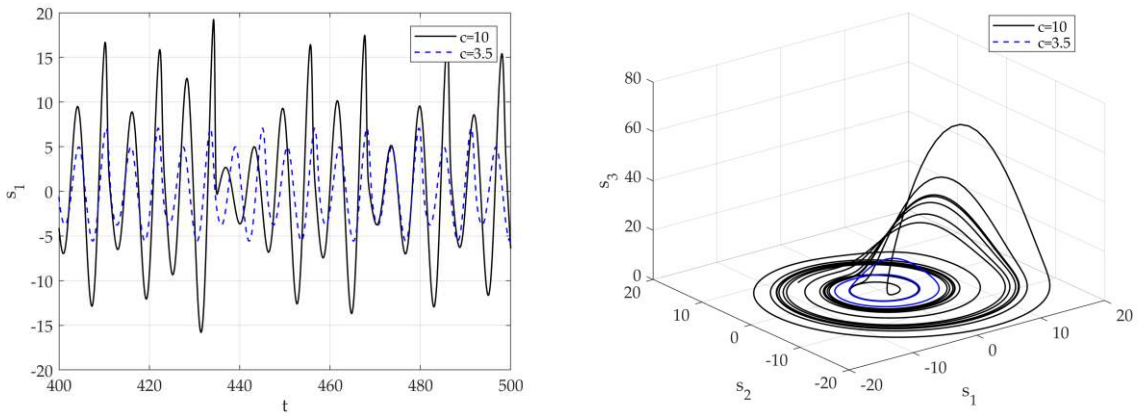

Figure4: Dynamic solutions for the Rossler model for various c (a) time analysis (b) 3-D phase portrait.

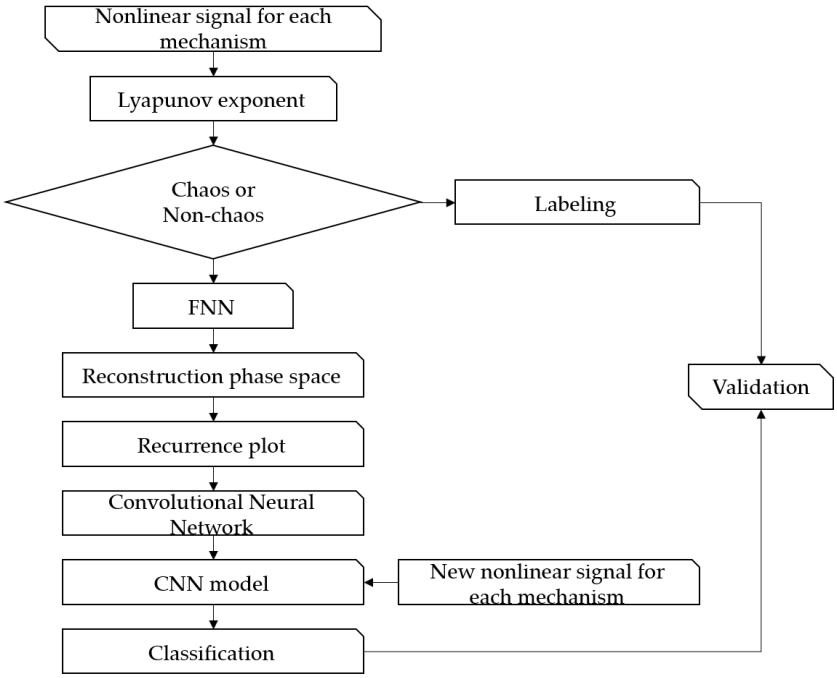

Figure5: Flow diagram of the proposed methodology

As shown in the flow diagram, the proposed method classifies the characteristics of the nonlinear vibration signals not included in learning after learning a dataset of nonlinear vibration signals composed of images using the CNN architecture. In other words, the focus of this study was to learn the vibrating signal visualized based on RP by machine learning and to distinguish between the causes of vibration, such as friction or impact and chaotic characteristics. Details of the proposed method are as follows. First, the nonlinear time series data of the parametric deterministic dynamic system was obtained by numerical analysis using the Runge-Kutta method. The Lyapunov exponent was calculated for the time series data and chaos was determined. The image visualization method of the vibration signal used the FNN algorithm to determine the embedding dimension and reconstruct the phase space. The reconstructed signal was expressed as an unthresholded RP to visualize the dynamic characteristics. Finally, the dataset composed of the visualized signals was trained by the CNN model and verified using the Lyapunov exponent.

The architecture is structured relatively simply. However, GAP was used instead of Fully Connected (FC) to activate the CAM in the last layer. GAP is relatively less accurate than FC [35]. On the other hand, the purpose of this paper was to show that even if the S&R model is chaotic, it is possible to classify it through deep learning using imaged vibration signals. Hence, the architecture was constructed simply with the aim of approximately 90% accuracy. For preliminary analysis, Table 1 lists the layer type of the CNN model, filter size, and shape of each layer. Figure 6 presents a flow diagram of the Rossler system's CNN model.

315 **Table 1.** CNN model summary

Layer (Type)	Output Shape	Param #
Conv2d	(None, 200, 200, 32)	896
Batch normalization	(None, 200, 200, 32)	128
Max pooling 2d	(None, 100, 100, 32)	0
Conv2d_1	(None, 100, 100, 64)	18496
Batch normalization_1	(None, 100, 100, 64)	256
Max pooling 2d_1	(None, 50, 50, 64)	0
Conv2d_2	(None, 50, 50, 128)	73856
Batch normalization_2	(None, 50, 50, 128)	512
Max pooling 2d_2	(None, 25, 25, 128)	0
Conv2d_3	(None, 25, 25, 256)	295168
Batch normalization_3	(None, 25, 25, 256)	1024
Max pooling 2d_3	(None, 12, 12, 256)	0
Conv2d_4	(None, 12, 12, 512)	1180160
Global average pooling 2d	(None, 512)	0
Dense	(None, 2)	1026

316

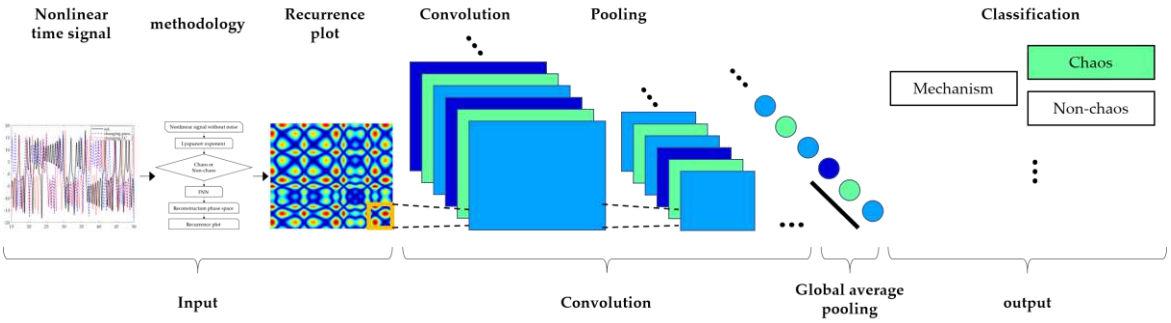

317
318 Figure 6: Flow diagram of CNN model

319

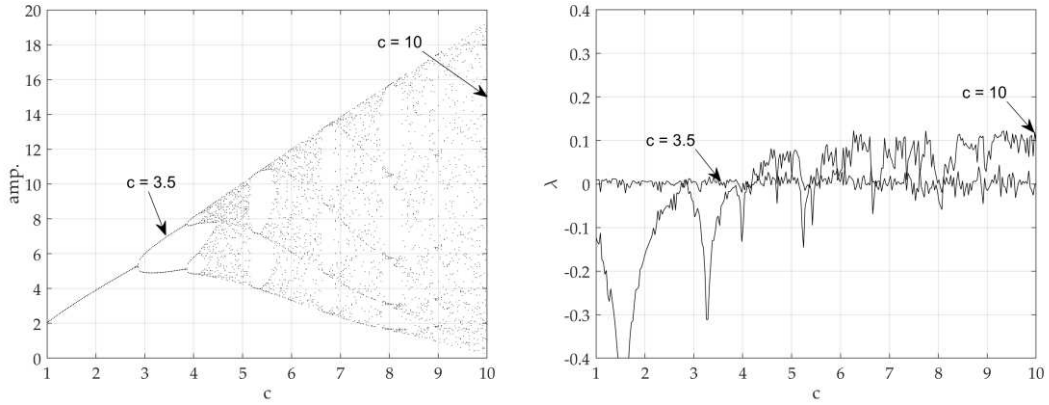

320
321 Figure 7: Chaotic analysis for Rossler model (a) bifurcation diagram of displacement (b) and largest
322 Lyapunov exponent with respect to c

Figure 7 presents the chaos analysis of the Rossler model. Figure 7 (a) is a bifurcation diagram of the Rossler's model for parameter c change, and Figure 6 (b) shows the corresponding Lyapunov exponents. The explanation of the critical c for the Lyapunov exponents of the Rossler model has been studied extensively. Briefly, to summarize this system, the first bifurcation appears near $c \approx 2.866$, and becomes period 2. The bifurcation appears again near $c \approx 3.86$ and becomes period 4. In other words, chaos occurs as period-doubling occurs at each point. As shown in Figure 4, if the time analysis result is $c = 3.5$, chaos is expressed as period 2, and $c = 10$. This agrees well with the time analysis results. In 3D phase space, the Lyapunov exponent has four types of attractors: stable fixed points ($\lambda_i < 0$, $i = 1,2,3$), stable limit cycles ($\lambda_1 < 0$, $\lambda_i < 0$, $i = 2,3$), stable two-torus ($\lambda_1 = \lambda_2 = 0$, $\lambda_i < 0$, $i = 3$), and strange attractors ($\lambda_1 > 0$). In the calculated system, however, only the classification of the S&R model and the existence of chaos were classified (Rossler system only distinguished between chaos and non-chaos). In other words, the strange attractor ($\lambda_1 > 0$) and dynamic characteristics of the deterministic dynamic system can be obtained from the flow of the proposed method, and an unthresholded recurrence plot was learned using CNN. Subsequently, an attempt was made to classify the signals and chaos generated by the S&R model that were not used for training. Figure 8 shows the visualized chaos and non-chaos signals for the randomly extracted Rossler model.

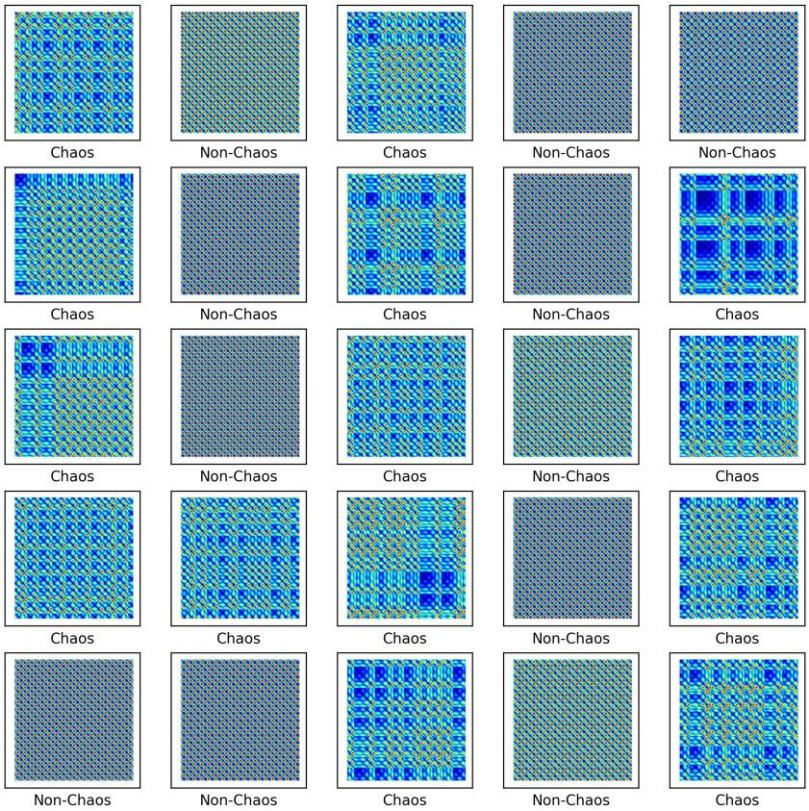

Figure 8: Unthresholded recurrence plot of the Rossler model

Image classification using CNN has developed many sophisticated models that transcend the human cognitive abilities, but the design of a sophisticated architecture was not the goal of the present study. Therefore, the architecture is composed of a simple five-level structure, as shown in Table 1. Each step includes the convolution layer, activation function, and pooling layer. The proposed model comprises five convolution layers with a 32-3x3 filter, 64-3x3 filter, 128-3x3 filter, 256-3x3 filter, and 512-3x3 filter in each step. As mentioned earlier, RP is a tool to visualize the recurrence characteristics of a dynamic system. The filter size was set as small as possible because the chaos system can occur within a very short interval. In addition, three max-pooling layers were used. Through five convolution layers, the feature map classifies the features of the image into six classes. To use CAM, GAP was used instead of the FC layer as the last layer. Softmax was used as the activation function of the output value. One of the gradient-based optimization methods was used. The Adam optimizer is an optimization function based on the gradient descent algorithm and was used to achieve faster convergence [37]. The weight initialization is one of the fundamental problems. Incorrect weight setting causes many problems, such as convergence problems and local minima. LeCun initialization follows a Gaussian distribution and uniform distribution of weight initialization for effective backpropagation [38]. Xavier initialization sets the initial weight depending on the number of previous and next nodes [39]. This is the most generalized method, but the output value shows inefficient results when used in the ReLU function. He initialization was developed to compensate for this [26]. For the weight initialization in the proposed CNN model, the He initialization method following a Gaussian distribution was used.

The Rossler model consisted of 3200 datasets and 200 x 200-pixel images. The intervals of the time step for the ODE and orthonormalization for the Lyapunov exponent were 0.05 and 0.1, respectively. The dataset is usually divided into three parts. The 3200 datasets were divided into 70% for the training dataset and 30% of the test dataset. The validation dataset consisted of 30% of the training dataset. Table 2 lists the dataset samples used for training. The errors due to sequential datasets were removed by shuffling the dataset because the images are generated sequentially for parameter analysis.

Table 2. Dataset split ratio for the Rossler model

Data	Percentage	Number of samples
Training	56 %	2240
Validation	14 %	560
Testing	30 %	1200

Figure 9 shows the results of a numerical experiment for the proposed procedure. Chaos characteristics were found in the training dataset for 2240. At the same time, it was verified through 560 validation data in each epoch. After that, the tests were performed on 1200 testing datasets on the trained CNN model. The batch size was set to 10, and the learning rate of the optimization function was 0.0001. Figure 9 (a), (b) shows the accuracy and loss function of the training data and validation data for each epoch. As shown in the learning result, the accuracy showed a logarithmic function and converged to approximately 100, and the loss also showed a negative exponential function and converged close to zero. The accuracy and loss of validation data and the training data almost

coincide, suggesting that the training proceeded well without overfitting. This suggests that the proposed procedure detects the chaos characteristics of the Rossler model well. In addition, 1200 testing datasets that were not used for training were also classified with 99% accuracy.

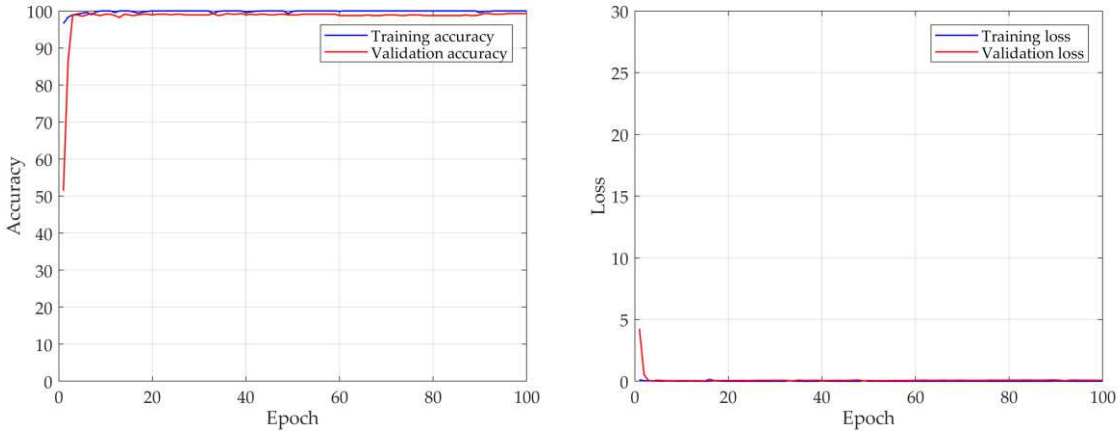

Figure 9: Results of the numerical experiment for the Rossler model (a) accuracy (b) and loss curves over 100 epochs

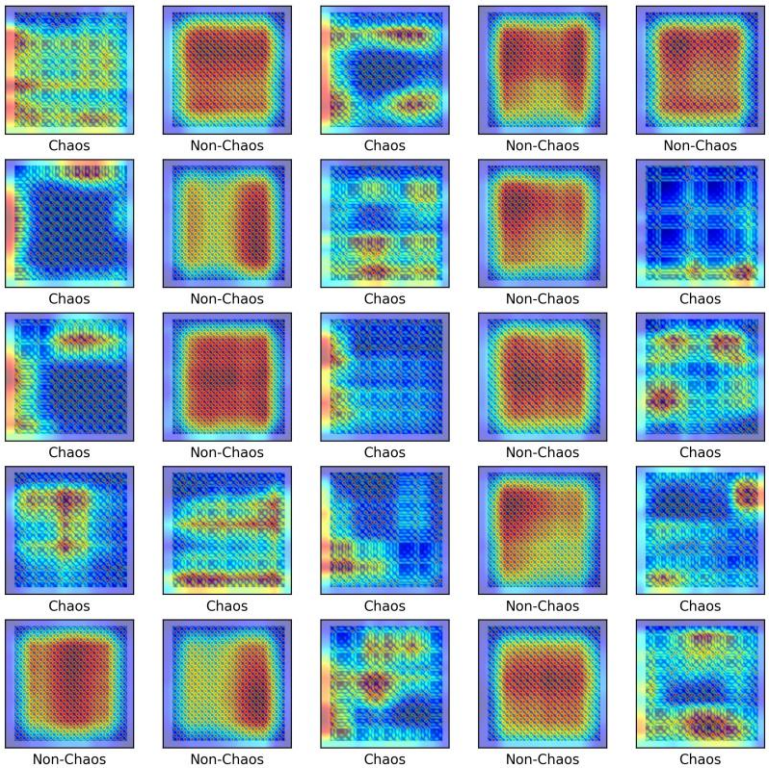

Figure 10: Class activation mapping for the Rossler model

Figure 10 shows the heat map using CAM. The heat map shows the spatial importance for each class, and red is the most important part. As shown in the heat map, when the iteration of the Rossler

392 model is non-chaos, the characteristics of the image tend to be uniform and symmetrical, and the
393 chaos is irregular.

394 In the Rossler model, the cycle is long and clearly expressed for the set control parameters.
395 Therefore, the visualized repetition was distinguished easily. On the other hand, the S&R model,
396 which includes the friction force and impact force, contains extreme nonlinearities so that the
397 repeatability can be very complex. Here, because the rattle problem contains discontinuities, the
398 Lyapunov exponent was calculated by considering Muller's method. The squeak problem has a
399 continuity, including creep, so the Lyapunov was calculated as a continuous dynamic problem.

400

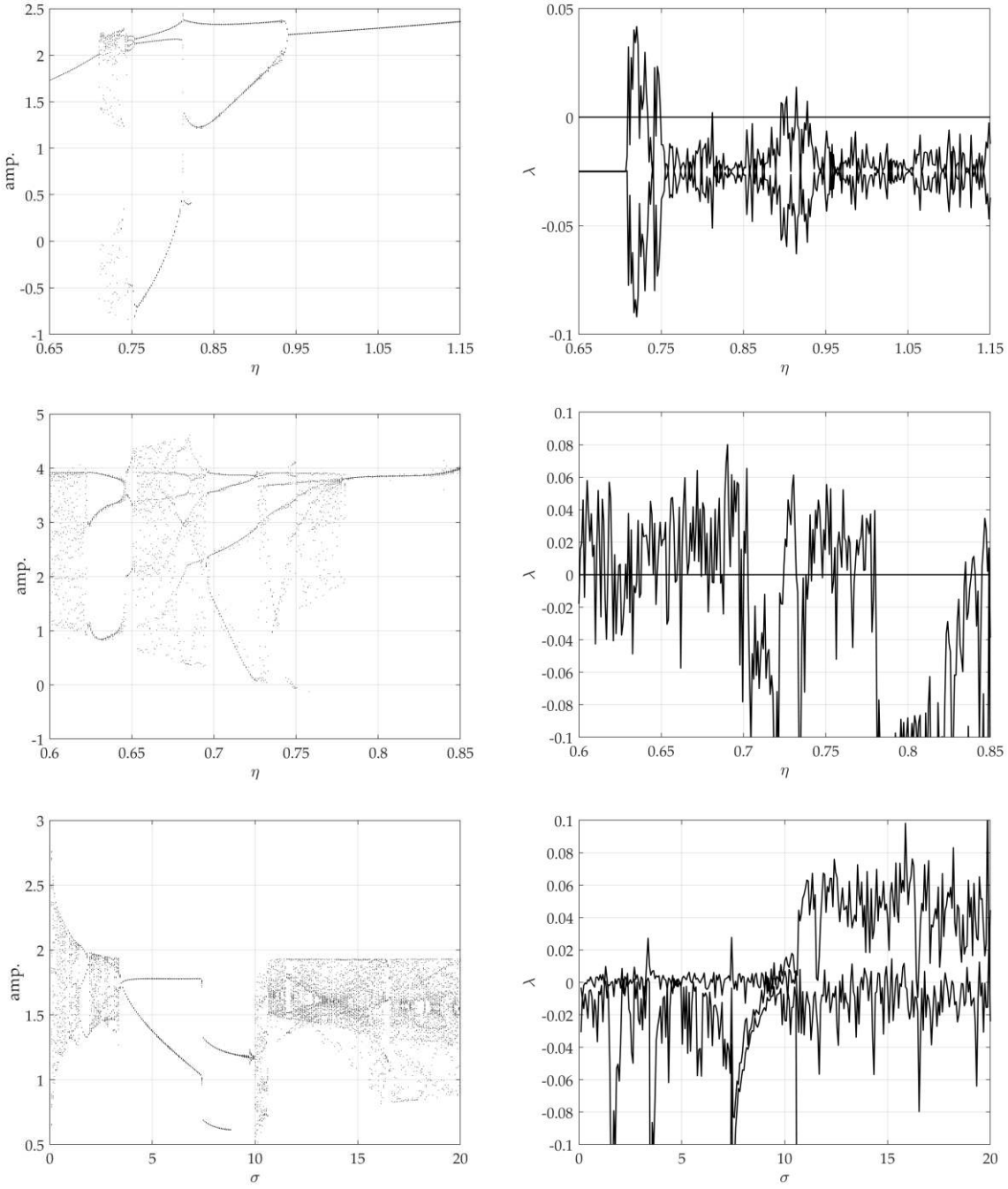

Figure 11: Chaotic analysis for the S&R model (a) bifurcation diagram of displacements (b) and largest Lyapunov exponent; for rattle model with respect to η (c) bifurcation diagram of displacements (d) and largest Lyapunov exponent; for single-mode squeak model with respect to η (e) bifurcation diagram of displacements (f) and largest Lyapunov exponent; for multi-modes squeak model with respect to σ

Figure 11 shows the results of chaotic analysis for the model control parameters corresponding to

each model. Figure 11 (a) is the calculation result of the largest Lyapunov exponent of the rattle model, and Figure 11 (b) shows the corresponding bifurcation diagram. The other parameters and initial conditions are $r=2$, $\xi=0.05$, $k_h=100$, and $\mathbf{u}_0=\begin{bmatrix}0.4 & -1.1 & 0\end{bmatrix}^{\mathbf{T}}$. Figure 11 (c) and (d) show the Lyapunov exponent calculation result for the control parameter of the single-mode squeak model and the corresponding bifurcation diagram. Figure 11 (c) and (d) show the Lyapunov exponent calculation result for the control parameter of the single-mode squeak model and the corresponding bifurcation diagram. The other parameters and initial conditions are $V=2$, $n_0=2.5$, $\beta=0.002$, $\mu_s=0.5$, $\mu_k=0.1$, $h=1$, $\alpha=65$, and $\mathbf{v}_0=\begin{bmatrix}0.1 & 1.2 & 0\end{bmatrix}^{\mathbf{T}}$. Figure 11 (e) and (f) present the Lyapunov exponent calculation result and bifurcation diagram for the control parameter of the multi-modes squeak model. Other parameters and initial conditions were $V=1$, $n_0=2.5$, $\beta=\beta_1=0$, $\mu_s=0.5$, $\mu_k=0.3$, $h=1$, $\alpha=65$, $\gamma=0.1$, and $\mathbf{w}_0=\begin{bmatrix}0.1 & 0.1 & 0.1 & 1.1\end{bmatrix}^{\mathbf{T}}$. In this study, only each model and chaotic characteristics were distinguished, so other detailed types of attractors were not considered. The analysis results show that the S&R model changes with extreme nonlinearity in the largest Lyapunov exponent for the change in the control parameter.

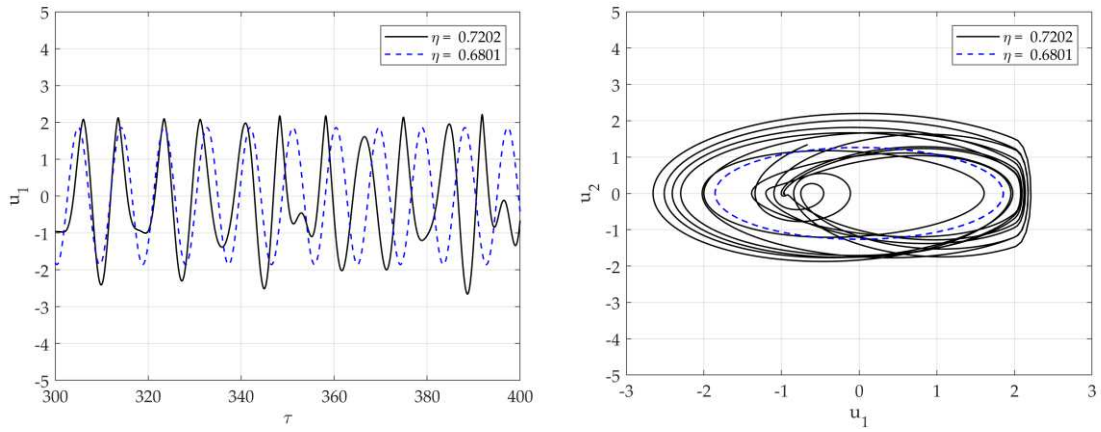

Figure 12: Dynamic solutions for the rattle model for various η (a) time analysis, (b) Phase portrait corresponding to (a).

As mentioned earlier, Figures 12, 13, and 14 present the representative attractors of each system divided into chaos and non-chaos, and show the rattle, single-mode squeak, and multi-mode squeak models, respectively. Figure 12 (a) and (b) show the time series plot and phase portrait of displacement for the rattle model in $\eta=0.7202$ and $\eta=0.6801$. The dotted line oscillates constantly, and the solid line vibrates with an irregular amplitude. In phase space at $\eta=0.6801$, it produces one stable limit cycle without impact and oscillates stably. On the other hand, in $\eta=0.7202$, the system includes impact, and the trajectory appears without a specific period. In other words, it expresses chaos.

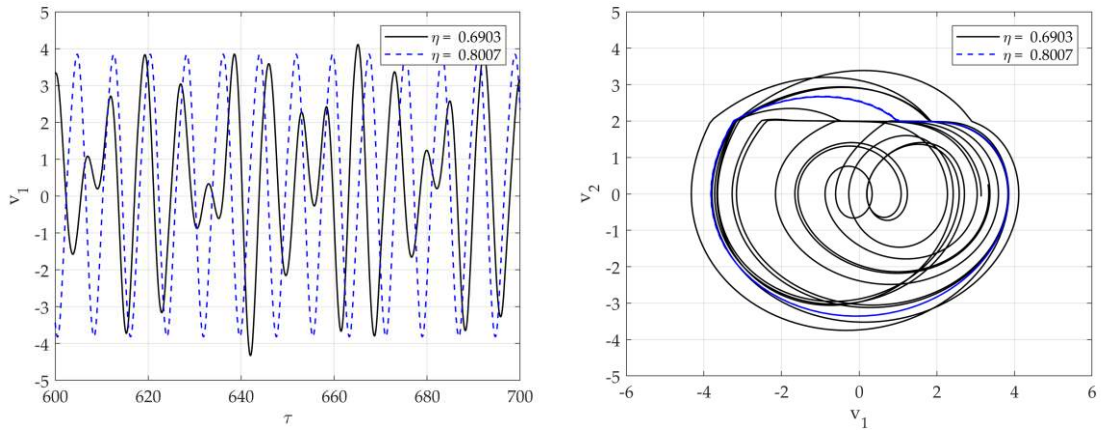

Figure 13: Dynamic solutions for single-mode squeak model for various η (a) time analysis, (b) Phase portrait corresponding to (a)

Figure 13 (a) and (b) show the time series plot and phase portrait of displacement for the single-mode squeak model in $\eta = 0.8007$ and $\eta = 0.6903$. The dotted line oscillates constantly, and the solid line vibrates with an irregular amplitude. In the phase plot, the flat phase means the stick phase in the stick-slip. When $\eta = 0.8007$ produces an unstable limit cycle in phase space, and it vibrates unstable for 1 period within the limit cycle. On the other hand, in $\eta = 0.6903$, the system produces an unstable limit cycle and generates chaos without a constant cycle.

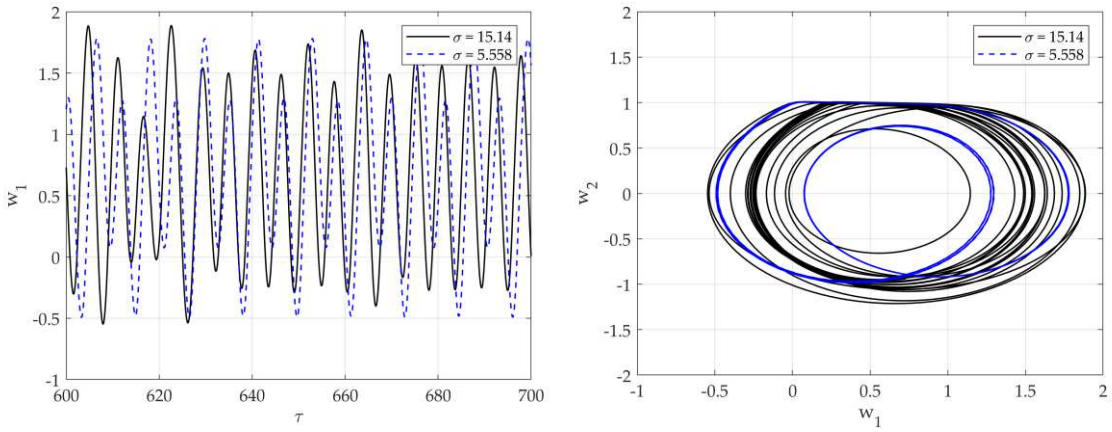

Figure 14: Dynamic solutions for multi-mode squeak model for various σ (a) time analysis, (b) Phase portrait corresponding to (a).

Figures 14 (a) and (b) show the time series plot and phase portrait of displacement for the multi-mode squeak model in $\sigma = 15.14$ and $\sigma = 5.558$. The dotted line constantly oscillates with two amplitudes, and the solid line oscillates with an irregular amplitude. In phase space at $\sigma = 15.14$, it

vibrates unstably for two periods within the limit cycle. On the other hand, at $\sigma = 5.558$, the system generates an unstable limit cycle and generates chaos.

The S&R model was classified into six classes to distinguish between chaos and non-chaos, and an unthresholded RP was shown. Here, the six classes were divided into the rattle, single-mode squeak and multi-modes squeak, and chaos and non-chaos for each model. Table 2 lists the dataset sample, and Figure 15 presents a part of the training dataset.

Table 2. Dataset split for the S&R model

Data	Percentage	Number of samples
Training	56 %	4160
Validation	14 %	1040
Testing	30 %	1800

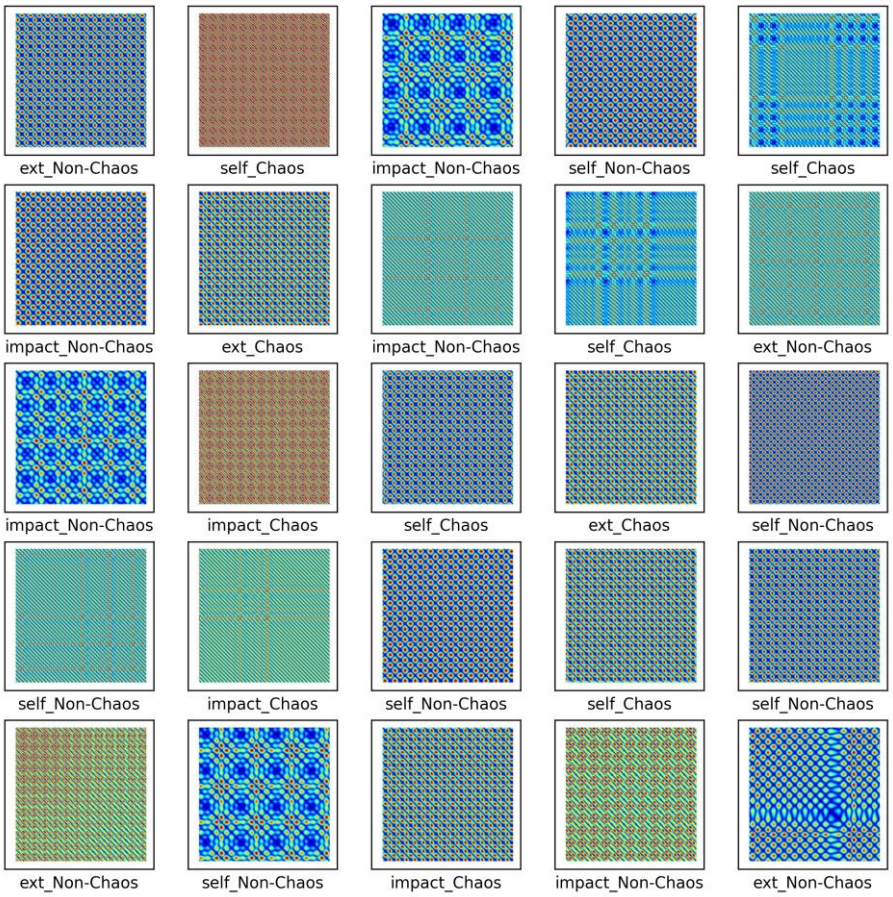

Figure 15: Unthresholded RP for the S&R model

As shown in Figure 15, images by chaos and images by non-chaos are always vibrating, so repetition appears in a complex form. Six thousand data were used in the total dataset and consisted

of 200 x 200-pixel images. To escape the local minima and converge to a lower loss, and prevent overfitting, the learning rate was adjusted for each specific step using a callback function. Each step consisted of five convolution layers with 32-2x2 filter, 64-2x2 filter, 128-2x2 filter, 256-2x2 filter, and 512-2x2 filter.

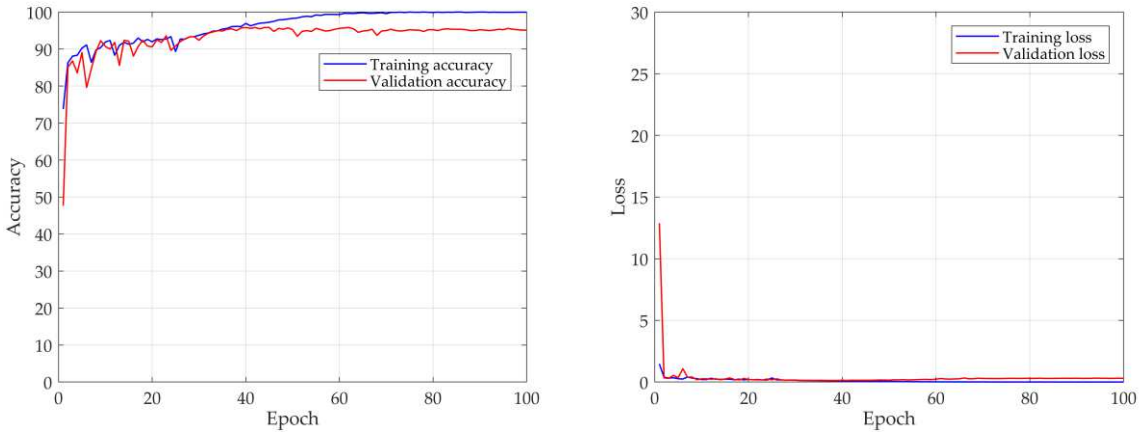

Figure 16: Results of the numerical experiment for the S&R model (a) accuracy (b) and loss curves over 100 epochs

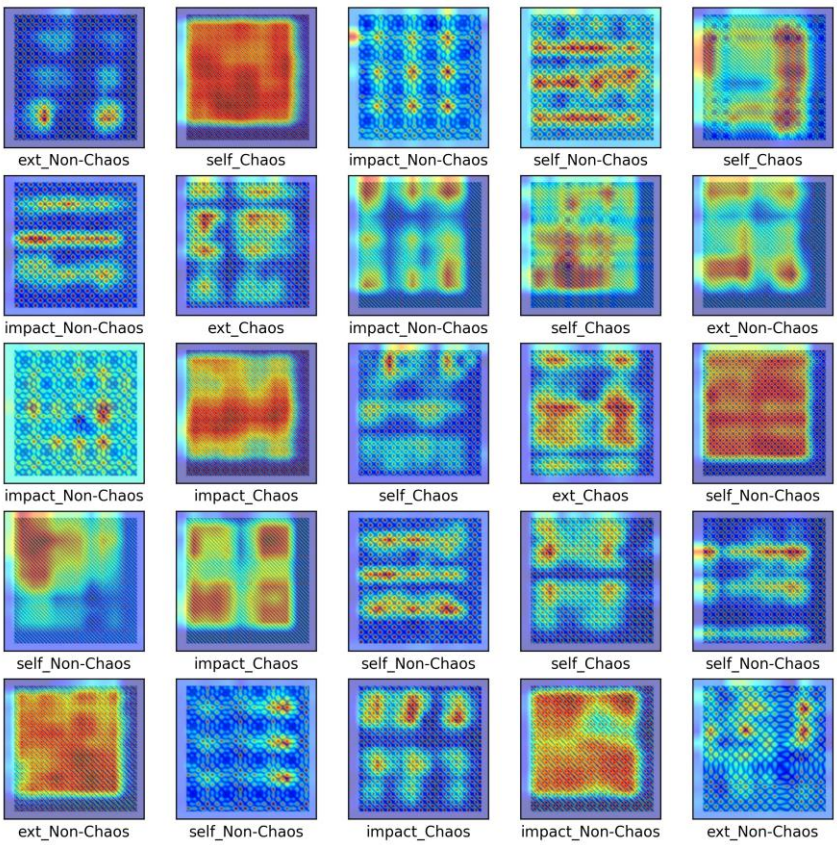

Figure 17: Class activation map for the S&R model

Figure 16 shows the results of the numerical experiment. The validation loss and accuracy do not decrease until 20 epochs but escape from the local minima by adjusting the learning rate. This shows that the learning rate is adjusted again at 70 epochs and converges with a certain accuracy and loss. In the final test, the model of each system and the chaos problem were classified with approximately 90% accuracy. Figure 17 shows the characteristics of the nonlinear vibration signal of each system for data extracted randomly by CAM. The areas of difference for the recurrence characteristics for each model were detected successfully using deep learning. The proposed procedure can classify the nonlinear vibration characteristics generated in the mechanical system with high accuracy. In other words, the causes of complex signals can be classified due to nonlinear vibrations generated in mechanical systems with high accuracy. This shows that the characteristics of the complex signals that humans cannot recognize can be classified with high accuracy by a CNN.

4. Discussion and future work

Visualization was performed with the proposed method for the vibration signals with extreme nonlinearity occurring in different models. The CNN was used to classify the S&R model and its chaotic characteristics. This result was verified by calculating the Lyapunov exponent for each model. The chaotic characteristics can distinguish the signals generated in a deterministic system by calculating the Lyapunov exponent, but calculating this is very complex. The signal visualization method analyzes the dynamic signals, but signals containing nonlinearity are complicated for engineers to analyze. In other words, complex signals are difficult to classify by human cognitive ability. Therefore, a procedure for classifying S&R models, including chaos and non-chaos, was proposed and verified with approximately 91% accuracy using a simple CNN model. Future work will study a more complex model to analyze signals with added noise.

Data Availability

The datasets generated during the current study are available from the corresponding author on reasonable request.

Declaration of Competing Interest

The authors declare that they have no known competing financial interests or personal relationships that could have appeared to influence the work reported in this paper.

Reference

[1] Lee, G. J., Kim, K., Kim, J.: Development of an algorithm to automatically detect and distinguish squeak and rattle noises. SAE Technical Paper. (2015) No. 2015-01-2258. https://doi.org/10.4271/2015-01-2258

[2] Cerrato-Jay, G., Gabiniewicz, J., Gatt, J., Pickering, D. J.: Automatic detection of buzz, squeak and rattle events. SAE transactions. (2001) 1763-1770. https://www.jstor.org/stable/44731038

[3] Wang, Y. S., Lee, C. M., Kim, D. G., Xu, Y.: Sound-quality prediction for nonstationary vehicle interior noise based on wavelet pre-processing neural network model. J. Sound Vib. 299, 933-947 (2007)

[4] Kavarana, F., Rediers B.: Squeak and rattle-state of the art and beyond. SAE Noise and Vibration Conference. (1999) SAE Paper 1999-01-1728. https://doi.org/10.4271/1999-01-1728

[5] Zheng, X., Agarwal, V., Liu, X., Balachandran, B.: Nonlinear instabilities and control of drill-string stick-slip vibrations with consideration of state-dependent delay. J. Sound Vib. 473, 115235 (2020)

[6] Arvin, H., Arena A., Lacarbonara, W.: Nonlinear vibration analysis of rotating beams undergoing parametric instability: Lagging-axial motion, Mech. Syst. Signal Process. 144, 106892 (2020)

[7] Dong, C., Mo, J., Yuan, C., Bai, X., Tian, Y.: Vibration and noise behaviors during stick–slip friction, Tribol. Lett. 67, 1-12 (2019)

[8] Kang, J., Krousgrill, C. M., Sadeghi, F.: Comprehensive stability analysis of disc brake vibrations including gyroscopic, negative friction slope and mode-coupling mechanisms. J. Sound Vib. 324, 387-407 (2009)

[9] Niknam, A., Farhang, K.: Vibration instability in a large motion bistable compliant mechanism due to stribeck friction. J. Vib. Acoust. 140, 061017 (2018)

[10] Nam, J., Do, H., Kang, J.: Investigation of friction induced vibration in lead screw system using FE model and its experimental validation. Appl. Acoust. 122 98-106 (2017)

[11] Ouenzerfi, G., Massi, F., Renault, E., Berthier, Y.: Squeaking friction phenomena in ceramic hip endoprosthesis: Modeling and experimental validation. Mech. Syst. Signal Process. 58 87-100 (2015)

[12] Oberst, S., Lai, J. C. S.: Nonlinear transient and chaotic interactions in disc brake squeal. J. Sound Vib. 342, 272-289 (2015)

[13] Li, Z., Cao, Q., Nie, Z.: Stick-slip vibrations of a self-excited SD oscillator with Coulomb friction. Nonlinear Dyn. 102, 1419-1435 (2020)

[14] Wei, D., Ruan, J., Zhu, W., Kang, Z.: Properties of stability, bifurcation, and chaos of the tangential motion disk brake. J. Sound Vib. 375, 353-365 (2016)

[15] Kang, J.: Lyapunov exponent of friction-induced vibration under smooth friction curve. J. Mech. Sci. Tech. 32, 3563-3567 (2018)

[16] Müller, P. C.: Calculation of Lyapunov exponents for dynamic systems with discontinuities. Chaos Solitons Fractals. 5, 1671-1681 (1995)

[17] Wolf, A., Swift, J. B., Swinney, H. L., Vastano, J. A.: Determining Lyapunov exponents from a time series. Phys. D. 16 285-317 (1985)

[18] Serweta, W., Okolewski, A., Blazejczyk-Okolewska, B., Czolczynski, K., Kapitaniak, T.: Lyapunov exponents of impact oscillators with Hertz′ s and Newton′ s contact models. Int. J. Mech. Sci. 89 194-206 (2014)

[19] Serweta, W., Okolewski, A., Blazejczyk-Okolewska, B., Czolczynski, K., Kapitaniak, T.: Mirror hysteresis and Lyapunov exponents of impact oscillator with symmetrical soft stops. Int. J. Mech. Sci. 101 89-98 (2015)

[20] Kang, J.: Calculation of Lyapunov exponents in impacted beam on distributed contact. J. Sound Vib. 431, 295-303 (2018)

[21] Awrejcewicz, J., Krysko, A. V., Erofeev, N. P., Dobriyan, V., Barulina, M. A., Krysko, V. A.: Quantifying chaos by various computational methods. Part 1: simple systems, Entropy. 20, 175 (2018)

[22] Astaf'eva, N. M.: Wavelet analysis: basic theory and some applications, Phys. Usp. 39, 1085 (1996)

[23] Marwan, N., Romano, M. C., Thiel, M., Kurths, J.: Recurrence plots for the analysis of complex systems. Phys. rep. 438, 237-329 (2007)

[24] Cao, L.: Practical method for determining the minimum embedding dimension of a scalar time series. Phys. D. 110, 43-50 (1997)

[25] Kennel, M. B., Brown, R., Abarbanel, H. D.: Determining embedding dimension for phase-space reconstruction using a geometrical construction, Phys. Rev. A. 45, 3403 (1992)

[26] March, T. K., Chapman, S. C., Dendy, R. O.: Recurrence plot statistics and the effect of embedding. Physica D. 200, 171-184 (2005)

[27] Wallot, S., Mønster, D.: Calculation of average mutual information (AMI) and false-nearest neighbors (FNN) for the estimation of embedding parameters of multidimensional time series in matlab. Front. Psychol. 9, 1679 (2018)

[28] Butusov, D. N., Karimov, A. I., Pesterev, D. O., Tutueva, A. V., Okoli, G.: Bifurcation and recurrent analysis of memristive circuits. 2018 IEEE Conference of Russian Young Researchers in Electrical and Electronic Engineering (EIConRus) (2018) 178-183. https://doi.org/10.1109/EIConRus.2018.8317059

[29] Zou, Y., Donner, R. V., Donges, J. F., Marwan, N., Kurths, J.: Identifying complex periodic windows in continuous-time dynamical systems using recurrence-based methods. Chaos 20. 4, 043130 (2010)

[30] He, K., Zhang, X., Ren, S., Sun, J.: Deep residual learning for image recognition. Proc. IEEE Conf. Comput. Vis. Pattern Recognit. (2016) 770-778

[31] Hsueh, Y., Ittangihala, V. R., Wu, W. B., Chang, H. C., Kuo, C. C.: Condition monitor system for rotation machine by CNN with recurrence plot. Energies. 12, 3221 (2019).

[32] Nam, J., Kang, J.: Classification of Chaotic Signals of the Recurrence Matrix Using a Convolutional Neural Network and Verification through the Lyapunov Exponent. Appl. Sci.-Basel. 11, 77 (2021)

[33] Parker, T.S., Chua, L.: In Practical Numerical Algorithms for Chaotic Systems. Springer-Verlag New York, New York, 1989

[34] Thiel, M., Romano, M.C., Kurths, J., Meucci, R., Allaria, E., Arecchi, F.T.: Influence of observational noise on the recurrence quantification analysis. Phys. D. 171, 138–152 (2002)

[35] Zhou, B., Khosla, A., Lapedriza, A., Oliva, A., Torralba, A.: Learning deep features for discriminative localization. Proceedings of the IEEE Conference on Computer Vision and Pattern Recognition (CVPR) (2016) 2921-2929. https://doi.org/10.1109/CVPR.2016.319

587 [36] Barrio, R., Blesa, F., Serrano, S.: Qualitative analysis of the Rössler equations: Bifurcations of limit
588 cycles and chaotic attractors. Phys. D. 238, 1087–1100 (2009)

589 [37] Kingma, D.P., Ba, J.: Adam: A method for stochastic optimization, Proceedings of the
590 International Conference on Learning Representations (ICLR) (2015)

591 [38] LeCun, Y.A., Bottou, L., Orr, G.B., Müller, K.: Efficient backprop, Springer, Berlin Heidelberg,
592 1998

593 [39] Glorot, X., Bengio, Y.: Understanding the difficulty of training deep feedforward neural networks.
594 Proceedings of the thirteenth international conference on artificial Intelligence and Statistics (AISTATS)
595 (2010) 249–256.